Plasmon-shaped polarization gating for high-order-harmonic generation

Feng Wang,[1] Lixin He,[1] Jiawei Chen,[1] Baoning Wang,[1] Xiaosong Zhu,[1,*] Pengfei Lan,[1,†] and Peixiang Lu[1,2]

[1]*School of Physics and Wuhan National Laboratory for Optoelectronics, Huazhong University of Science and Technology, Wuhan 430074, China*

[2]*Laboratory of Optical Information Technology, Wuhan Institute of Technology, Wuhan 430205, China*

We present a plasmon-shaped polarization gating for high-order-harmonic generation by using a linearly polarized laser field to illuminate two orthogonal bow-tie nanostructures. The results show that when these two bow-tie nanostructures have nonidentical geometrical sizes, the transverse and longitudinal components of the incident laser field will experience different phase responses, thus leading to a time-dependent ellipticity of laser field. For the polarizing angle of incident laser field in the range from 45° to 60°, the dominant harmonic emission is gated within the few optical cycles where the laser ellipticity is below 0.3. Then sub-50-as isolated attosecond pulses (IAPs) can be generated. Such a plasmon-shaped polarization gating is robust for IAP generation against the variations of the carrier-envelope phases of the laser pulse. Moreover, by changing the geometrical size of one of the bow-tie nanostructures, the electron dynamics can be effectively controlled and the more efficient supercontinuum as well as IAP can be generated.

I. INTRODUCTION

High-order-harmonic generation (HHG) through the interaction of intense laser pulses with atomic or molecular gases has been widely investigated for producing coherent extreme ultraviolet radiations and attosecond pulses. These ultrashort pulses offer unprecedented temporal resolution in observing and controlling electron and nuclear dynamics in atoms [1], molecules [2–4], and solids [5,6]. Due to the great importance in the attosecond metrology [7], how to generate an isolated attosecond pulse (IAP) has been one of the most exciting areas in attosecond science. One of the mechanisms to generate IAPs is to manipulate the ionization and acceleration steps of electrons by shaping the laser field [8–10], such as the use of two-color and multicolor fields, etc. More than that, the high harmonic yield depends sensitively on the ellipticity of laser fields. It has demonstrated that polarization gating composed of left- and a right-circular pulses with a certain delay can gate the recombination step of electrons within a few optical cycles and then generate IAPs [11–17]. Very recently, with this method, a 53-as IAP was produced in the experiment [18]. However, the conventional polarization gating needs accurate control of the carrier envelope phase (CEP) of the laser pulse and a delay between the left- and right-circular laser field components, which will undoubtedly add to the complexity of the experiments.

Recently, an alternative way to generate high harmonics by utilizing a plasmon-enhanced laser field has attracted wide attention [19–23]. The plasmonic field enhancement results from the collective oscillations of free conduction electrons in the noble metal nanostructure, i.e., surface plasmon resonance (SPR) [24]. When the resonance wavelength of the nanostructure is matched with the wavelength of the incident laser field, the intensity of the laser field can be boosted up by more than 2 orders of magnitude [25]. It allows one to attain the

laser intensities needed for HHG (10 TW/cm^2) directly from a moderate-power femtosecond oscillator and therefore offers a possibility for generating the high-repetition-rate attosecond pulses [20,26]. By using an array of bow-tie nanostructures, Kim *et al.* [19] first experimentally demonstrated that the high harmonics with wavelengths from 47 to 117 nm can be generated. However, due to the inefficient harmonic emissions, the plasma atomic lines can overpower the harmonic signals [27]. Therefore, the result of Kim's experiment has been subject to an intense controversy since it was reported [28,29]. Fortunately, alternative approaches to realize efficient plasmon-driven HHG, such as employing different kinds of nanostructure [20] or using a solid tip as the HHG emitter instead of gas atoms, have been explored [21]. In the region where the HHG processes take place, the enhanced field is spatially inhomogeneous. By using the linearly spatial-dependent laser fields, researchers have discovered some characteristics of plasmon-driven HHG [30–35], for instance, the selection of quantum paths and the extension of the cutoff, etc. In addition, recent research shows that SPR can also abruptly change the phase of the incident laser field, which gives a way to modulate the polarization of the laser field on an ultrafast time scale [36–39].

In this paper, we demonstrate a plasmon-shaped polarization gating for HHG. By using two orthogonal bow-tie nanostructures with different geometrical sizes, the transverse and longitudinal components of the incident linearly polarized laser field experience different phase shifts, which leads to a time-dependent ellipticity of the laser field. For the polarizing angle of the incident laser field in the range from 45° to 60°, the dominant harmonic emission is gated within the few optical cycles where the laser ellipticity is under 0.3, then sub-50-as IAPs can be produced. The presented plasmon-shaped polarization gating for IAP generation is insensitive to the CEP of the laser pulse. Moreover, as the geometrical size of one of the bow-tie nanostructure changes, the electron dynamics can be controlled and the efficiency of the supercontinuum can be significantly enhanced. Compared with the conventional polarization gating, the plasmon-shaped polarization gating is

---

*zhuxiaosong@mail.hust.edu.cn
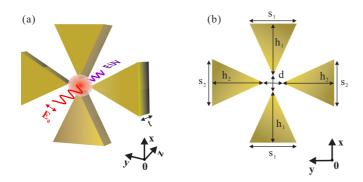
†pengfeilan@mail.hust.edu.cn

063418-1

FIG. 1. (a), (b) Geometry and front view of two orthogonal bow-tie nanostructures. These two nanostructures are placed in the $x-y$ plane and the input pulse propagates along the z axis.

helpful to relax the requirement of control of both the CEPs of the laser pulse and the delay between the left- and right-circular laser components for ultrashort IAP generation. On the other hand, due to the subwavelength size of the nanostructure, the plasmon-shaped polarization gating is more easy to integrate into compact platforms.

II. THEORETICAL MODEL

A. Finite-difference time-domain simulation of plasmonic fields

In our calculation, we solve the three-dimensional Maxwell's equations for the propagation of plasmonic field in the nanostructure. The Maxwell's curl equations are given by

$$\nabla \times \overrightarrow{H}(x,y,z,t) = \frac{\partial \overrightarrow{D}(x,y,z,t)}{\partial t} + \overrightarrow{J}(x,y,z,t), \quad (1)$$

$$\nabla \times \overrightarrow{E}(x,y,z,t) = -\frac{\partial \overrightarrow{B}(x,y,z,t)}{\partial t} - \overrightarrow{J}_m(x,y,z,t), \quad (2)$$

where $\overrightarrow{E}$ and $\overrightarrow{H}$ are the electric and magnetic vectors, and $\overrightarrow{D}$ and $\overrightarrow{B}$ are the electric displacement and magnetic inductive. $\overrightarrow{J}$ and $\overrightarrow{J}_m$ are electric and magnetic current densities.

Equations (1) and (2) are solved by the finite-difference time-domain (FDTD) method in Cartesian coordinates. Here, we use the software Lumerical FDTD SOLUTIONS that implements the FDTD method to calculate the plasmonic field $\overrightarrow{E}$ [40]. Figures 1(a) and 1(b) illustrate the geometry and front view of the two orthogonal bow-tie nanostructures. The height h_1, side s_1, thickness t, and gap d are kept as constants: 160 nm, 75 nm, 50 nm, and 20 nm. The height h_2 and side s_2 are specified below. These two nanostructures are made of gold, whose wavelength-dependent complex dielectric constants are taken from Palik data [41]. The damage threshold of incident laser intensity for gold is about 5 TW/cm² [42]. To calculate the time-dependent plasmonic field, a Gaussian laser field with wavelength of 810 nm, duration of 5 fs, and field amplitude normalized to 1 V/m was used as the incident laser pulse. The actual input field intensity is 1 TW/cm². The spatial range in our simulation is $450 \times 450 \times 100$ nm with a spatial step of 1 nm. The total simulation time is 100 fs with a time step of 5 as. Based on our simulation, we find

that in our case the z component of the plasmonic fields $E_z(x,y,z,t)$ are always equal to 0. Therefore, the longitudinal (x-direction) and transverse (y-direction) plasmonic field components $E_x(x,y,z,t)$ and $E_y(x,y,z,t)$ are extracted for driving the HHG process.

B. Plasmon-driven high-order-harmonic generation

We then solve the time-dependent Schrödinger equation (TDSE) to model the plasmon-driven HHG [43,44]. The TDSE in two spatial dimensions is expressed as

$$i\frac{\partial \psi(x,y,t)}{\partial t} = H(t)\psi(x,y,t)$$

$$= \left[-\frac{1}{2}\frac{\partial^2}{\partial x^2} - \frac{1}{2}\frac{\partial^2}{\partial y^2} + V_{\text{atom}}(x,y) \right.$$

$$\left. + V(x,y,t) \right] \psi(x,y,t), \quad (3)$$

where $H(t)$ and $\psi(x,y,t)$ are the Hamiltonian and the electron wave function, respectively. The Coulomb potential $V_{\text{atom}}(x,y)$ is described by

$$V_{\text{atom}}(x,y) = -\frac{1}{\sqrt{x^2 + y^2 + \varepsilon}}, \quad (4)$$

and the soft core parameter ε is equal to 0.12 for the gas medium of neon. The potential $V(x,y,t)$ represents the interaction of the atomic electron and laser field. It is given by

$$V(x,y,t) = E_0[E_x(x+x_0,y+y_0,z_0,t)x$$
$$+ E_y(x+x_0,y+y_0,z_0,t)y], \quad (5)$$

where E_0 is the actual input field amplitude. $E_x(x+x_0,y+y_0,z_0,t)$ and $E_y(x+x_0,y+y_0,z_0,t)$ are the longitudinal and transverse plasmonic field components extracted from the Lumerical FDTD SOLUTIONS. (x_0,y_0,z_0) represents the coordinate of the target point. In this work, the harmonic spectra are calculated at the points $x_0 = -4$, $y_0 = 0$, and $z_0 = 25$ nm, where the harmonic cutoff energy is highest.

Equation (3) is solved by the split-operator method. The generated harmonics can be calculated by the time-dependent dipole acceleration along the x and y directions: $a_x(t)$ and $a_y(t)$, which is given by

$$a_x(t) = \frac{d^2\langle x \rangle}{dt^2} = -\langle \psi(t)|[H(t),[H(t),x]]|\psi(t)\rangle, \quad (6)$$

$$a_y(t) = \frac{d^2\langle y \rangle}{dt^2} = -\langle \psi(t)|[H(t),[H(t),y]]|\psi(t)\rangle. \quad (7)$$

The harmonic spectrum is then obtained by Fourier transforming the dipole acceleration:

$$aq_x = \left| \frac{1}{\tau} \int_0^\tau a_x(t)\exp(-iq\omega t) \right|^2, \quad (8)$$

$$aq_y = \left| \frac{1}{\tau} \int_0^\tau a_y(t)\exp(-iq\omega t) \right|^2, \quad (9)$$

where q is the harmonic order. Based on our simulation, we find that the y component of the harmonic spectrum amplitude is much smaller than the x component of the
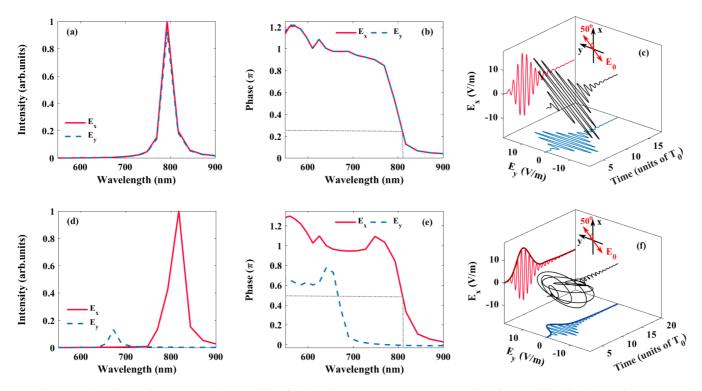
FIG. 2. (a), (b) Plasmonic resonance characteristics for the IG nanostructure. In (a), every data is normalized by the maximum spectral intensity of $E_x(x_0,y_0,z_0)$. (c) Temporal profiles of $E_x(x_0,y_0,z_0,t)$ (light red line), $E_y(x_0,y_0,z_0,t)$ (light blue line), and $E(x_0,y_0,z_0,t)$ (black line). (d)–(f) Same as (a)–(c), but for the NIG nanostructure. The dark red and dark blue lines in (f) are envelopes of $E_x(x_0,y_0,z_0,t)$ and $E_y(x_0,y_0,z_0,t)$, respectively. Here, the input field E_0 is linearly polarized and α is 50°.

harmonic spectrum amplitude. Therefore, we only consider the x component in our work.

III. RESULTS AND DISCUSSION

In Fig. 2(a) we investigate the inherent resonance behavior of two orthogonal bow-tie nanostructures with identical geometrical size, i.e., $h_2 = h_1 = 160$ nm and $s_2 = s_1 = 75$ nm (IG nanostructure, for short). Figure 2(d) is the result with nonidentical geometrical size, i.e., $h_2 = 100$ nm and $s_2 = 92$ nm (NIG nanostructure, for short). The inherent resonance behavior of the nanostructure is obtained by sweeping the wavelength of the laser field. The wavelength where the spectral intensity reaches the maximum is usually defined as the resonance wavelength of the nanostructure. Here, the input field E_0 is linearly polarized. The angle between the polarization direction of E_0 and the positive-x axis (polarizing angle α, for short) is 50°. When the two orthogonal bow-tie nanostructures have identical geometry [Fig. 2(a)], the resonance wavelengths for the x and y components of plasmonic fields $E_x(x_0,y_0,z_0)$ and $E_y(x_0,y_0,z_0)$ are both about 790 nm, whereas when changing h_2 to 100 nm and s_2 to 92 nm [Fig. 2(d)], the resonance peak of $E_y(x_0,y_0,z_0)$ shows a remarkable blue shift relative to that in Fig. 2(a). The resonance wavelengths for $E_x(x_0,y_0,z_0)$ and $E_y(x_0,y_0,z_0)$ are approximately equal to 815 nm and 670 nm, respectively. The obvious separation of x/y componential resonance peaks indicates that longitudinal and transverse input field components experience different spectral responses. Figures 2(b) and 2(e) present the phase charac-

istics of $E_x(x_0,y_0,z_0)$ and $E_y(x_0,y_0,z_0)$ in the IG and NIG nanostructures. For the incident laser field with a wavelength of 810 nm, the spectral phases of $E_x(x_0,y_0,z_0)$ and $E_y(x_0,y_0,z_0)$ are the same in the IG case. But they present a phase difference of 0.5 π in the NIG case. In Figs. 2(c) and 2(f), we simulate the temporal profiles of $E_x(x_0,y_0,z_0,t)$, $E_y(x_0,y_0,z_0,t)$, and $E(x_0,y_0,z_0,t)$ in the IG and NIG nanostructures. In the IG case,
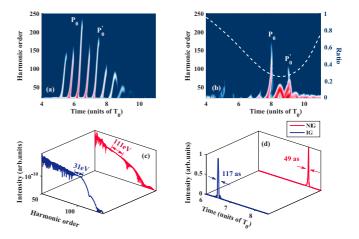

FIG. 3. (a), (b) Time-frequency distribution of HHG from the IG and NIG nanostructures. (c), (d) Harmonic spectra and temporal profiles of IAPs in the IG and NIG nanostructures. White dotted line in (b) is the time-dependent ellipticity of $E(x_0,y_0,z_0,t)$. Here, α is 50°.

$E_x(x_0,y_0,z_0)$ and $E_y(x_0,y_0,z_0)$ have same phase, and therefore the $E(x_0,y_0,z_0,t)$ is still linearly polarized, while in the NIG case, the polarization direction of $E(x_0,y_0,z_0,t)$ varies rapidly with time due to the phase difference between the $E_x(x_0,y_0,z_0)$ and $E_y(x_0,y_0,z_0)$.

Next, we investigate the HHG from the gas-exposed IG and NIG nanostructures in Fig. 3. The high harmonics are generated by the interaction of the plasmonic field with gas medium neon injected into the gap of the nanostructure. In Fig. 3(a), we show the harmonic intensity as a function of harmonic order and radiation time (time-frequency distribution of HHG) in the IG case. One can see that the harmonic emissions occur in every half-optical cycle of the plasmonic field and only the short quantum paths are generated. The vanishing of long quantum paths is due to the strong wave-packet diffusion effect in the spatially inhomogeneous field. The energy difference between the highest peak P_0 and second highest peak P_0' decides the bandwidth of the supercontinuum. Thus a supercontinuum with a bandwidth of 31 eV is generated in the region from H190 to H210 [see Fig. 3(c)]. By synthesizing the supercontinuum, an IAP with a duration of 117 as is obtained [see Fig. 3(d)]. Figure 3(b) shows the time-frequency distribution of HHG in the NIG nanostructure. One can see that the harmonic emissions only occur at $t = 8\,T_0$, $8.5\,T_0$, $9\,T_0$ (where T_0 is the optical cycle of the plasmonic field). To clarify this phenomenon, we show the time-dependent ellipticity $\xi(t)$ of $E(x_0,y_0,z_0,t)$, which is presented by the white dotted line in Fig. 3(b). $\xi(t)$ is defined as the ratio between the envelopes of $E_x(x_0,y_0,z_0,t)$

and $E_y(x_0,y_0,z_0,t)$. In the region from $8\,T_0$ to $9\,T_0$, $\xi(t)$ exhibits a valley where the ellipticities are all below 0.3. Such a characteristic of the plasmonic field is analogous to that of the conventional polarization gating [11]. Since the harmonic yield drops dramatically with the increase of $\xi(t)$, the harmonic emissions at $8\,T_0 \leqslant t \leqslant 9\,T_0$ are much stronger than those at $t < 8\,T_0$ and $t > 9\,T_0$. This result coincides well with the time-frequency distribution of HHG. In addition, in the NIG case, the energy difference between the highest and second highest peaks P_0 and P_0' is 111 eV, which is much larger than that in IG case [Fig. 3(c)]. Therefore, a shorter IAP with a duration of 49 as is produced in the NIG case, as shown in Fig. 3(d).

Further, we investigate the influence of polarizing angle α on the plasmon-shaped polarization gating. Figures 4(a)–4(d) show the time-dependent plasmonic fields with α of 30°, 45°, 60°, and 75°. Figures 4(e)–4(h), 4(i), and 4(j) are the corresponding time-frequency distribution of HHG, harmonic spectra, and temporal profiles of IAPs. The white dotted lines in Figs. 4(e)–4(h) are the time-dependent ellipticity of $E(x_0,y_0,z_0,t)$. With α of 30° [Fig. 4(e)], $\xi(t)$ is less than 0.3 in the region from $7\,T_0$ to $10\,T_0$, where the dominant harmonic emissions are generated. In this case, the supercontinuum of HHG is from the contribution of the highest peak P_0, whose bandwidth is 30 eV, as shown in Fig. 4(i). By synthesizing this supercontinuum, an IAP with a duration of 123 as is obtained [see Fig. 4(j)]. When α is 45° or 60° [Figs. 4(f) and 4(g)], the harmonic emissions that occur at $t < 8\,T_0$ and $t > 9\,T_0$ are inappreciable. This phenomenon is similar to that with α of
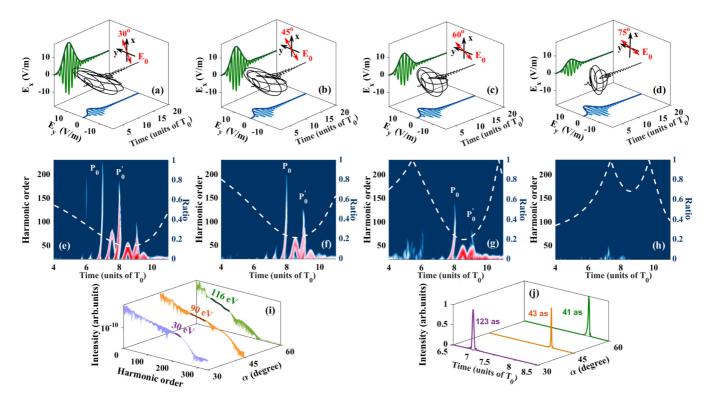

FIG. 4. (a)–(d) and (e)–(h): Plasmonic fields and time-frequency distributions of HHG in the NIG nanostructures with α of 30°, 45°, 60°, and 75°. White dotted lines in (e)–(h) are the time-dependent ellipticity of $E(x_0,y_0,z_0,t)$. (i), (j) Harmonic spectra and temporal profiles of IAPs with α of 30°, 45°, and 60°.
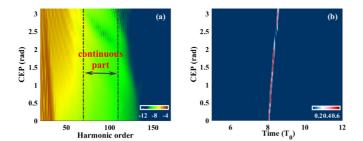
FIG. 5. (a) CEP dependence of HHG from NIG nanostructure with α of $60°$. The color represents harmonic intensity, which is plotted in logarithmic coordinates. (b) Temporal profiles of attosecond pulses generated by selecting continuous harmonics in (a).
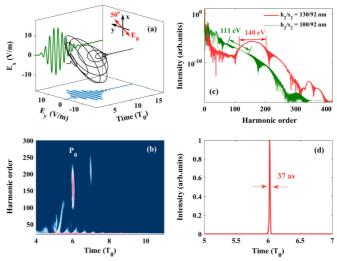

FIG. 6. (a)–(d) Plasmonic fields, time-frequency distribution of HHG, harmonic spectrum (red line), and temporal profiles of IAP in the NIG nanostructure with h_2 of 130 nm and s_2 of 92 nm. The green line in (c) is the harmonic spectrum with h_2 of 100 nm and s_2 of 92 nm.

$50°$ in Fig. 3(b). From Figs. 4(i) and 4(j), one can see that the bandwidth of supercontinuum and duration of IAP are 90 eV and 43 as for $\alpha = 45°$, and are 116 eV and 41 as for $\alpha = 60°$. When α is increased to $75°$ [Fig. 4(h)], the ellipticity $\xi(t)$ is larger than 0.4 in each half-optical cycle of the plasmonic field. Thus the harmonic emissions are inefficient throughout the laser pulse.

Figure 5(a) shows the harmonic spectra generated in a gas-exposed NIG nanostructure with the CEP of the incident laser field changing from 0 to π. Here, α is $60°$. For most CEPs, the continuous harmonics are generated in the range from 108 eV (70th) to 170 eV (110th). By superposing the harmonics in the continuous part, we obtain the temporal profiles of attosecond pulses as presented in Fig. 5(b). One can clearly see that only one main attosecond pulse is generated at each CEP value and the obtained pulse durations are rather stable.

In Fig. 6, we extend the height of the transverse bow-tie nanostructure to 130 nm and investigate the influence of the geometrical size of the nanostructure on the plasmon-shaped polarization gating. Here, α is $50°$. From Fig. 6(b), one can see that the electron dynamics is controlled to produce a noticeable radiation peak at 6 T_0. It is different from the case with h_2 of 100 nm in Fig. 3(b), where an obvious radiation peak is located at 8 T_0. Moreover, compared to the supercontinuum in the 100-nm case [green line in Fig. 6(c)], the bandwidth (140 eV) of the supercontinuum is broadened by 29 eV and the intensity of the supercontinuum is enhanced by 2 orders of magnitude in the 130-nm case [red line in Fig. 6(c)]. From Fig. 6(b), one can also see that the attochirp of HHG from peak P_0 is quite small. Therefore, a near Fourier-transform-limited IAP with a duration of 37 as is generated by synthesizing the supercontinuum in the 130-nm case [see Fig. 6(d)].

Finally, it must be noted that in our calculation, we consider only one unit, including two bow-tie nanostructures, rather than an array of such units. For an array placed perpendicular to the propagation axis, each single unit acts as a pointlike source. Since the thickness of the array is much smaller than the incident laser wavelength and the size of the array is usually much smaller than the beam waist of the Gaussian laser field in realistic setups [19], the longitudinal and transverse phase mismatching [45] of HHG may be neglected. Then the

harmonic emissions coming from each unit will be coherent superposition.

IV. CONCLUSION

In conclusion, we have presented a plasmon-shaped polarization gating for HHG by using a linearly polarized laser field to illuminate two orthogonal bow-tie nanostructures. The results show that when the two bow-tie nanostructures have identical geometrical size, the transverse and longitudinal components of the incident laser field experience the same spectral responses and then the output laser field is still linearly polarized. For the nonidentical geometrical sizes of these two bow-tie nanostructures, the transverse and longitudinal components of the incident laser field present different phase shifts, thus leading to a time-dependent ellipticity of the plasmonic field. Further simulations based on the two-dimension TDSE show that when the polarizing angle α is in the range from $45°$ to $60°$, the dominant harmonic emission is gated within the few optical cycles where the laser ellipticity is below 0.3. Then broadband supercontinua at the plateau are produced, which support the generation of sub-50-as IAPs. Such a plasmon-shaped polarization gating is robust for the IAP generation against the variations of CEPs. Moreover, by adjusting the geometrical size of the transverse bow-tie nanostructure, the electron dynamics can be effectively controlled and the more efficient supercontinuum as well as IAP can be generated.

ACKNOWLEDGMENT

[1] E. Goulielmakis, Z. Loh, A. Wirth, R. Santra, N. Rohringer, V. S. Yakovlev, S. Zherebtsov, T. Pfeifer, A. M. Azzeer, M. F. Kling, S. R. Leone, and F. Krausz, Nature (London) **466**, 739 (2010).

[2] P. Lan, M. Ruhmann, L. He, C. Zhai, F. Wang, X. Zhu, Q. Zhang, Y. Zhou, M. Li, M. Lein, and P. Lu, Phys. Rev. Lett. **119**, 033201 (2017).

[3] J. C. Baggesen and L. B. Madsen, Phys. Rev. Lett. **104**, 043602 (2010).

[4] D. Wang, X. Zhu, X. Liu, L. Li, X. Zhang, P. Lan, and P. Lu, Opt. Express **25**, 23502 (2017); M. Qin and X. Zhu, Opt. Laser Technol. **87**, 79 (2017); M. He, Y. Zhou, Y. Li, and P. Lu, Opt. Quantum Electron. **49**, 232 (2017).

[5] N. Yoshikawa, T. Tamaya, and K. Tanaka, Science **356**, 736 (2017).

[6] X. Liu, X. Zhu, P. Lan, X. Zhang, D. Wang, Q. Zhang, and P. Lu, Phys. Rev. A **95**, 063419 (2017).

[7] M. Hentschel, R. Kienberger, Ch. Spielmann, G. A. Reider, N. Milosevic, T. Brabec, P. Corkum, U. Heinzmann, M. Drescher, and F. Krausz, Nature (London) **414**, 509 (2001).

[8] P. Lan, P. Lu, W. Cao, Y. Li, and X. Wang, Phys. Rev. A **76**, 051801(R) (2007); L. He, Y. Li, Q. Zhang, and P. Lu, Opt. Express **21**, 2683 (2013).

[9] T. Pfeifer, L. Gallmann, M. J. Abel, D. M. Neumark, and S. R. Leone, Opt. Lett. **31**, 975 (2006).

[10] S. A. Rezvani, Z. Hong, X. Pang, S. Wu, Q. Zhang, and P. Lu, Opt. Lett. **42**, 3367 (2017); Z. Hong, Q. Zhang, S. A. Rezvani, P. Lan, and P. Lu, Opt. Laser Technol. **98**, 169 (2018); Z. Hong, S. A. Rezvani, Q. Zhang, and P. Lu, Opt. Quantum Electron. **49**, 392 (2017).

[11] Z. Chang, Phys. Rev. A **70**, 043802 (2004).

[12] W. Hong, P. Wei, Q. Zhang, S. Wang, and P. Lu, Opt. Express **18**, 11308 (2010).

[13] Z. Chang, Phys. Rev. A **71**, 023813 (2005).

[14] Q. Zhang, P. Lu, W. Hong, Q. Liao, and S. Wang, Phys. Rev. A **80**, 033405 (2009).

[15] G. Sansone, E. Benedetti, F. Calegari, C. Vozzi, L. Avaldi, R. Flammini, L. Poletto, P. Villoresi, C. Altucci, R. Velotta, S. Stagira, S. D. Silvestri, and M. Nisoli, Science **314**, 443 (2006).

[16] H. Mashiko, S. Gilbertson, C. Li, S. D. Khan, M. M. Shakya, E. Moon, and Z. Chang, Phys. Rev. Lett. **100**, 103906 (2008).

[17] J. Li, X. Ren, Y. Yin, Y. Cheng, E. Cunningham, Y. Wu, and Z. Chang, Appl. Phys. Lett. **108**, 231102 (2016).

[18] J. Li, X. Ren, Y. Yin, K. Zhao, A. Chew, Y. Cheng, E. Cunningham, Y. Wang, S. Hu, Y. Wu, M. Chini, and Z. Chang, Nat. Commun. **8**, 186 (2017).

[19] S. Kim, J. Jin, Y.-J. Kim, I.-Y. Park, Y. Kim, and S.-W. Kim, Nature (London) **453**, 757 (2008).

[20] I.-Y. Park, S. Kim, J. Choi, D.-H. Lee, Y.-J. Kim, M. F. Kling, M. I. Stockman, and S.-W. Kim, Nat. Photon. **5**, 677 (2011).

[21] S. Han, H. Kim, Y. W. Kim, Y.-J. Kim, S. Kim, I.-Y. Park, and S.-W. Kim, Nat. Commun. **7**, 13105 (2016).

[22] F. Wang, W. Liu, L. He, L. Li, B. Wang, X. Zhu, P. Lan, and P. Lu, Phys. Rev. A **96**, 033407 (2017); H. Yuan, L. He, F. Wang, B. Wang, W. Liu, and Z. Hong, Opt. Quantum Electron. **49**, 214 (2017).

[23] M. Blanco, C. Hernández-García, A. Chacón, M. Lewenstein, M. T. Flores-Arias, and L. Plaja, Opt. Express **25**, 14974 (2017).

[24] J. Chen, K. Wang, H. Long, H. Hu, X. Han, B. Wang, and P. Lu, Opt. Express **25**, 1296 (2017); S. Wang, B. Wang, C. Qin, K. Wang, H. Long, and P. Lu, Opt. Quantum Electron. **49**, 389 (2017); H. Long, L. Bao, A. A. Habeeb, and P. Lu, ibid. **49**, 345 (2017).

[25] S. A. Maier, Plasmonics: Fundamentals and Applications (Springer, New York, 2007).

[26] M. Krebs, S. Hädrich, S. Demmler, J. Rothhardt, A. Zaïr, L. Chipperfield, J. Limpert, and A. Tünnermann, Nat. Photon. **7**, 555 (2013).

[27] M. Sivis, M. Duwe, B. Abel, and C. Ropers, Nat. Phys. **9**, 304 (2013).

[28] M. Sivis, M. Duwe, B. Abel, and C. Ropers, Nature (London) **485**, E1 (2012).

[29] S. Kim, J. Jin, Y.-J. Kim, I.-Y. Park, Y. Kim, and S.-W. Kim, Nature (London) **485**, E1 (2012).

[30] J. A. Pérez-Hernández, M. F. Ciappina, M. Lewenstein, L. Roso, and A. Zaïr, Phys. Rev. Lett. **110**, 053001 (2013).

[31] J. Luo, Y. Li, Z. Wang, Q. Zhang, and P. Lu, J. Phys. B **46**, 145602 (2013); H. Yuan, F. Li, and H. Long, J. Opt. Soc. Am. B **34**, 2390 (2017).

[32] I. Yavuz, E. A. Bleda, Z. Altun, and T. Topcu, Phys. Rev. A **85**, 013416 (2012).

[33] M. F. Ciappina, J. Biegert, R. Quidant, and M. Lewenstein, Phys. Rev. A **85**, 033828 (2012); T. Shaaran, M. F. Ciappina, and M. Lewenstein, ibid. **86**, 023408 (2012); Y. Tikman, I. Yavuz, M. F. Ciappina, A. Chacón, Z. Altun, and M. Lewenstein, ibid. **93**, 023410 (2016).

[34] S. Choi, M. F. Ciappina, J. A. Pérez-Hernández, A. S. Landsman, Y.-J. Kim, S. C. Kim, and D. Kim, Phys. Rev. A **93**, 021405(R) (2016).

[35] L. He, Z. Wang, Y. Li, Q. Zhang, P. Lan, and P. Lu, Phys. Rev. A **88**, 053404 (2013); Z. Wang, P. Lan, J. Luo, L. He, Q. Zhang, and P. Lu, ibid. **88**, 063838 (2013).

[36] N. Yu, P. Genevet, M. A. Kats, F. Aieta, J.-P. Tetienne, F. Capasso, and Z. Gaburro, Science **334**, 333 (2011).

[37] Y. Yang, W. Wang, P. Moitra, I. I. Kravchenko, D. P. Briggs, and J. Valentine, Nano Lett. **14**, 1394 (2014).

[38] N. Yu, F. Aieta, P. Genevet, M. A. Kats, Z. Gaburro, and F. Capasso, Nano Lett. **12**, 6328 (2012).

[39] A. Pors, M. G. Nielsen, R. L. Eriksen, and S. I. Bozhevolnyi, Nano Lett. **13**, 829 (2013).

[40] E. Skopalová, D. Y. Lei, T. Witting, C. Arrell, F. Frank, Y. Sonnefraud, S. A. Maier, J. W. G. Tisch, and J. P. Marangos, New J. Phys. **13**, 083003 (2011); Z. Wang, B. Wang, H. Long, K. Wang, and P. Lu, J. Lightwave Technol. **35**, 2960 (2017); H. Huang, S. Ke, B. Wang, H. Long, K. Wang, and P. Lu, ibid. **35**, 320 (2017).

[41] E. D. Palik, Handbook of Optical Constants of Solids (Academic Press, New York, 1997).

[42] A. Husakou, S.-J. Im, and J. Herrmann, Phys. Rev. A **83**, 043839 (2011).

[43] Y. Li, M. Li, Y. Zhou, X. Ma, H. Xie, P. Lan, and P. Lu, Opt. Express **25**, 11233 (2017); Z. Wang, M. Li, Y. Zhou, P. Lan, and P. Lu, Sci. Rep. **7**, 42585 (2017).

[44] M. D. Feit, J. A. Fleck, Jr., and A. Steiger, J. Comput. Phys. **47**, 412 (1982).

[45] C. Hernández-García, I. J. Sola, and L. Plaja, Phys. Rev. A **88**, 043848 (2013).